

Anomalous temperature dependence of high-harmonic generation in Mott insulators

Yuta Murakami,¹ Kento Uchida,² Akihisa Koga,¹ Koichiro Tanaka,^{2,3} and Philipp Werner⁴

¹*Department of Physics, Tokyo Institute of Technology, Meguro, Tokyo 152-8551, Japan*

²*Department of Physics, Graduate School of Science,
Kyoto University, Sakyo-ku, Kyoto 606-8502, Japan*

³*Institute for Integrated Cell-Material Sciences, Kyoto University, Sakyo-ku, Kyoto, 606-8501, Japan*

⁴*Department of Physics, University of Fribourg, 1700 Fribourg, Switzerland*

(Dated: March 3, 2022)

High-harmonic generation (HHG) is a fundamental nonlinear optical phenomenon, whose scope has recently been extended from gases to solids. While HHG in semiconductors can be understood within a single-electron picture, the mechanisms underlying HHG in correlated materials remain to be clarified. Here, we theoretically reveal the crucial effect of spin-charge coupling on HHG in Mott insulators. In a system with antiferromagnetic correlations, the HHG signal is drastically enhanced with decreasing temperature, even though the gap increases and the production of charge carriers is suppressed. This anomalous behavior, which has also been observed in recent HHG experiments on Ca_2RuO_4 , originates from a cooperative effect between the spin-charge coupling and the thermal ensemble, and the resulting strongly temperature-dependent coherence between charge carriers. Our results demonstrate that correlations between different degrees of freedom, which are a characteristic feature of strongly correlated solids, have significant and nontrivial effects on nonlinear optical responses.

Introduction

High-harmonic generation (HHG) is a fundamental nonlinear optical phenomenon with potentially important technological applications. It was first reported in atomic gases three decades ago¹. HHG in gases is utilized in attosecond laser sources as well as spectroscopies, and provides the basis for attosecond science². The recent observation of HHG in solids, in particular semiconductors and semimetals³⁻¹⁰, extends the scope of the HHG research to condensed matter systems. HHG in semiconductors and semimetals can be well described by the dynamics of independent electrons in the periodic lattice potential (single-particle picture)¹¹⁻¹⁸, which enables the HHG spectroscopy of band information such as dispersion relations^{5,19}, Berry curvatures²⁰ and transition dipole moments²¹. On the other hand, the effects of electronic correlations are often taken into account phenomenologically and a detailed understanding of their role in solid-state HHG is lacking²²⁻²⁴. This understanding is however essential for the exploration of HHG in correlated materials, and it may enable future applications of the HHG spectroscopy to a wide range of materials, beyond semiconductors or semimetals.

The new research frontier of HHG in strongly correlated systems (SCSs) has attracted considerable interest both on the theoretical²⁵⁻³⁰ and experimental³¹⁻³³ sides. In contrast to semiconductors, which can be described in terms of electrons and holes, the driven state of SCSs involves various types of many-body elemental excitations. This makes the mechanism and features of HHG in SCSs nontrivial. Previous studies revealed the direct connection between many-body excitations and HHG in SCSs^{26,28,30}, and suggested possible spectroscopic applications of HHG to detect many-body states³⁰ as well as photoinduced phase transitions²⁵. On the other hand, very recently, it has been experimentally reported that

the Mott insulator Ca_2RuO_4 shows an unexpected exponential enhancement of the HHG signal with increasing gap size³³, see Fig. 1 a. Since a larger gap should suppress the excitation of charge carriers, this increase is opposite to the behavior expected for the semiconductor HHG³³. Such a counter-intuitive result calls for a deeper theoretical understanding of HHG in SCSs. A hallmark of SCSs is the coupling between different degrees of freedom, such as charges, orbitals and spins. These correlations are at the origin of rich physical properties observed in equilibrium SCSs^{34,35}. However, their role in highly nonlinear optical phenomena such as HHG is hardly known.

In this study, we reveal the crucial role of spin-charge coupling and the associated temperature effect on HHG in Mott insulators by theoretically analyzing the Hubbard model. Previous works showed that HHG in Mott insulators can be regarded as originating from the coherent dynamics of a pair of local many-body states – a doublon (doubly occupied state) and holon (empty state) – generated by strong fields, where the three-step model picture is applicable^{26,30}. The kinematics of doublons and holons is strongly correlated with spins, since their hopping disturbs the spin background. We demonstrate that this spin-charge coupling and its cooperation with thermal fluctuations strongly affect the coherence of doublon-holon pairs. This leads to a drastic enhancement of the intensity of the HHG signal and the cut-off frequency with decreasing temperature, even though the Mott gap is increased. Our numerical results qualitatively reproduce the strong temperature dependence of the HHG signal reported for the Mott insulator Ca_2RuO_4 , and its counter-intuitive dependence on the Mott gap, as shown in Fig. 1 b. These results demonstrate that strong correlations between active degrees of freedom in SCSs can result in peculiar behavior of highly nonlinear optical phenomena such as HHG. Our theoretic-

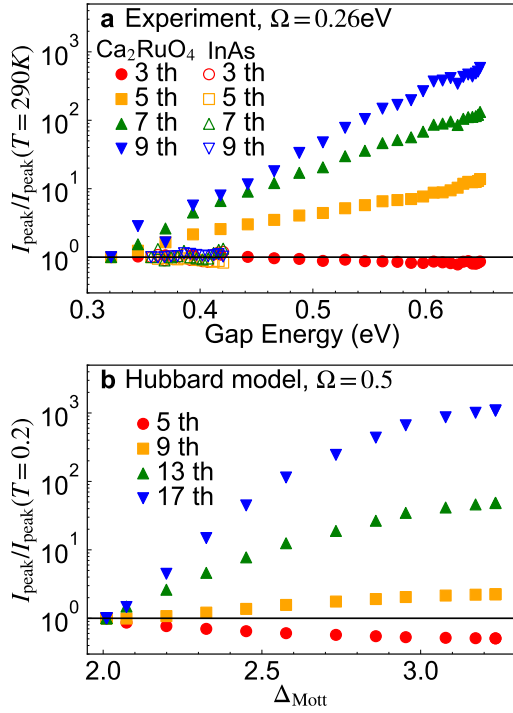


FIG. 1. **Anomalous HHG enhancement in Mott insulators.** **a** Experimental results of the HHG intensity at the indicated HHG peaks as a function of the optical gap for Ca_2RuO_4 (Mott insulator) and InAs (semiconductor), reproduced from Ref. 33. The temperature T is modified in the range of $T \in [290 \text{ K}, 50 \text{ K}]$, and these systems show a monotonic increase of the gap with decreasing temperature. The excitation frequency is $\Omega = 0.26 \text{ eV}$. **b** Theoretical results for the intensity at the indicated HHG peaks as a function of the Mott gap (Δ_{Mott}) for the single-band Hubbard model in the Mott insulating phase. Also in the calculations, the Mott gap increases with decreasing temperature. The results are obtained with nonequilibrium dynamical mean-field theory, and we consider the model on the Bethe lattice with bandwidth $W = 4$ and Hubbard interaction $U = 6$. The excitation frequency is $\Omega = 0.5$.

cal insights provide guiding principles for the exploration of HHG in SCSs, and suggest new ways of exploring the properties of SCSs far from equilibrium.

Results

Aniferromagnetic phase and spectral function of the single-band Hubbard model. In this study, we focus on the single-band Hubbard model, which is a standard model for SCSs. The Hamiltonian can be expressed as

$$\hat{H}(t) = -t_{\text{hop}} \sum_{\langle ij \rangle} e^{i\phi_{ij}(t)} \hat{c}_{i\sigma}^\dagger \hat{c}_{j\sigma} + U \sum_i \hat{n}_{i\uparrow} \hat{n}_{i\downarrow}, \quad (1)$$

where $\hat{c}_{i\sigma}^\dagger$ is the creation operator for an electron with spin σ at site i , $\langle ij \rangle$ indicates a pair of neighboring sites, and $\hat{n}_{i\sigma} = \hat{c}_{i\sigma}^\dagger \hat{c}_{i\sigma}$. t_{hop} is the hopping parameter and U is the onsite Coulomb interaction. The effect of electric

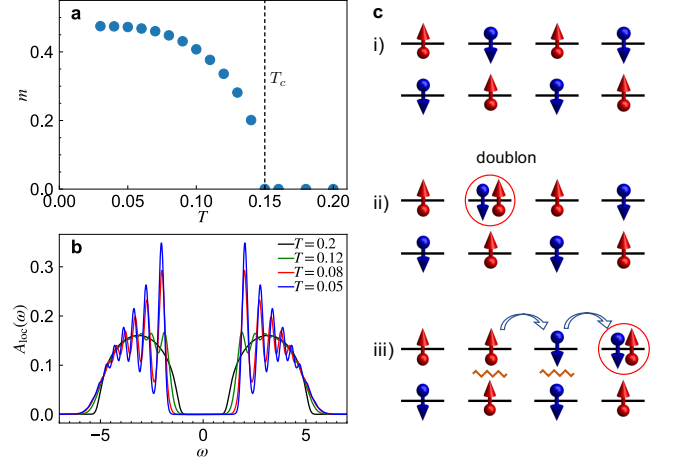


FIG. 2. **Equilibrium properties of the Hubbard model evaluated within dynamical mean-field theory.** **a** Temperature dependence of the magnetization, $m = |\langle \hat{n}_{i\uparrow} \rangle - \langle \hat{n}_{i\downarrow} \rangle|/2$. The vertical dashed line indicates the transition temperature T_c . **b** Local spectral function, $A_{\text{loc}}(\omega)$, for various temperatures. For **a** and **b**, we use $U = 6$ and consider the Bethe lattice. **c** Schematic pictures of the spin-charge coupling accompanying the kinematics of a doubton (circle). Panel i) shows the spin configuration of an antiferromagnetic state, ii) shows a doubton added to this state, and iii) shows the dynamics of the doubton, which disturbs the spin configuration (zigzag lines) at the cost of multiples of the exchange energy J_{ex} .

fields is included via a Peierls phase ϕ_{ij} , see Methods. We mainly use the nonequilibrium dynamical mean-field theory (DMFT)³⁶ to solve this problem, see Methods, and focus on the Bethe lattice for simplicity. The qualitatively same results are obtained for the two dimensional square lattice, as shown in the Supplemental Information (SI). In the following, we use the quarter of the bandwidth at $U = 0$ as the energy unit, and mainly consider $U = 6$. If we assume that our energy unit corresponds to 0.5 eV, the Mott gap ($\Delta_{\text{Mott}} \simeq 3$, see below) corresponds to 1.5 eV. This corresponds to the typical gap size of cuprates, which are often described by the single-band Hubbard model.

We consider the half-filled system, which becomes a Mott insulator for large enough U in equilibrium. While the Mott insulator can be realized in the paramagnetic (PM) phase, the system on the bipartite lattice exhibits an antiferromagnetic (AF) phase below the Néel temperature T_c . In Fig. 2 **a**, we show the temperature dependence of the staggered magnetization. The corresponding single-particle spectra are shown in Fig. 2 **b**. With decreasing temperature T , the Mott gap Δ_{Mott} increases. In the PM phase, the upper and lower Hubbard bands are smooth and featureless. On the other hand, in the AF phase, peak structures develop within the bands, indicating the formation of spin-polarons^{35,37}. When an electron is added to (removed from) the system, a doubton (holon) is created, see Fig. 2 **c**. When this doubton (holon) moves

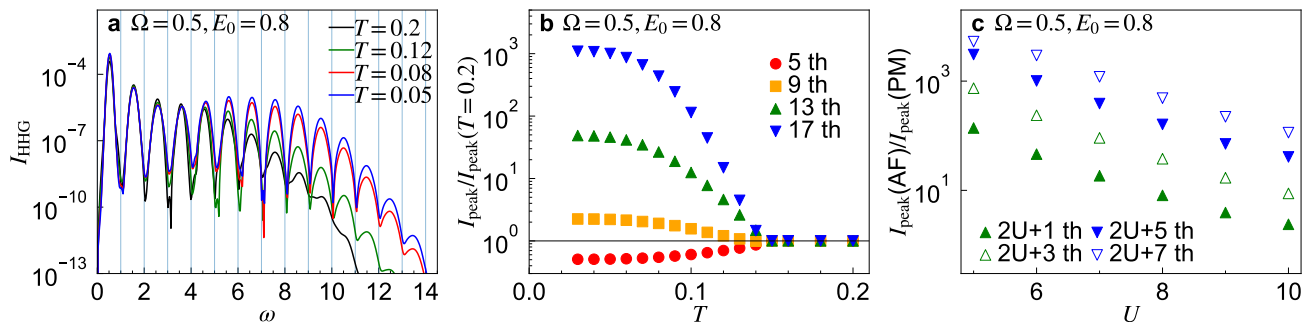


FIG. 3. **Temperature dependence of the HHG signal in Mott insulators.** **a** HHG spectra of the Mott insulator computed with DMFT for various temperatures. **b** The intensity at the peaks of the HHG spectra as a function of temperature. The peak intensity is normalized by the value at $T = 0.2$ (PM phase). For **a** and **b**, we use $U = 6$. **c** U -dependence of the increase ratio of the HHG peaks. In order to take into account the change of the Mott gap, we compare the $(2U + n)$ th HHG peaks. We note that the bandwidth of the upper and lower Hubbard bands is insensitive to U and the Mott gap scales almost linearly with U . We use $T = 0.2$ for the PM phase, while we use $T = 0.3/U$ for the AF state to take account of the change of $J_{\text{ex}} \propto \frac{1}{U}$. Note that the values of I_{peak} are almost saturated at these temperatures. In all cases, we consider a Gaussian electric field pulse centered at $t_0 = 75$ with the standard deviation $\sigma = 15$. The excitation frequency and the maximum field strength are $\Omega = 0.5$ and $E_0 = 0.8$, respectively.

around, it can disturb the spin background at the cost of multiples of the exchange energy $J_{\text{ex}} (= \frac{4t_{\text{hop}}^2}{U})$. This results in the strong spin-charge coupling in Mott insulators, and the spin-polaron is one manifestation of this coupling.

Temperature dependence of the high-harmonic generation. Now we discuss the role of the strong spin-charge coupling, i.e. the kinematics of doublons and holons accompanied by disturbance of the spin configurations, and its effect on highly nonlinear optical phenomena. We study the temperature dependence of HHG in Mott insulators excited with frequency Ω smaller than the Mott gap Δ_{Mott} . We mainly use $\Omega = 0.5$ in the following. If our energy unit corresponds to 0.5 eV, as mentioned above, this is a mid-infrared excitation with 0.25 eV, whose period T_p is about 16 fs. From the temperature dependence of the spectral functions, one would naively speculate that the HHG intensity is suppressed by lowering temperature, since the enhancement of the gap reduces the tunneling probability (see SI) and the formation of the spin-polarons suggests a reduced mobility of the charge carriers. However, the temperature dependence turns out to be completely opposite to this naive expectation.

Applying a Gaussian field pulse, we evaluate the HHG intensity $I_{\text{HHG}}(\omega)$ from the Fourier transformation of the current $J(t)$ as $I_{\text{HHG}}(\omega) = |\omega J(\omega)|^2$. We show the resultant HHG spectra for various temperatures in Fig. 3 **a** and plot the relative intensity of the HHG peaks as a function of temperature in Fig. 3 **b**. $I_{\text{HHG}}(\omega)$ is strongly enhanced above Δ_{Mott} and the width of the HHG plateau, where the intensity remains approximately constant over many harmonic orders, is enhanced as temperature is decreased, see Fig. 3 **a**. The increase in the ratio of HHG signals is larger for the higher harmonic peaks, see Fig. 3 **b**. Above T_c , the temperature depen-

dence of the HHG spectrum becomes very weak. As a function of the gap, the intensity increases almost exponentially, as illustrated in Fig. 1 **b**. Importantly, the DMFT results of the simple Hubbard model reproduce the qualitative features of the HHG spectrum measured in Ca_2RuO_4 ³³, see Fig. 1 **a**. We note that the characteristic temperature dependence of HHG can also be observed for higher excitation frequencies, where the ratio $\Delta_{\text{Mott}}/\Omega$ becomes closer to that in the experiments on Ca_2RuO_4 ³³, see SI. We also observe that the increase ratio is essentially determined by the emission photon energy ω (and not by the driving frequency), as it is the case in Ca_2RuO_4 ³³.

To obtain insights into the origin of the temperature dependence, we consider the U -dependence of the relative increase of the HHG signal, see Fig. 3 **c**. For large U the bandwidth of the upper and lower Hubbard bands is insensitive to U and the Mott gap scales almost linearly with U . Therefore, in order to focus on the contribution from the kinetic energy of the doublon-holon pair, we compare $I_{\text{HHG}}(\omega)$ for the same $\omega - U$. It turns out that the increase ratio monotonically decreases with increasing U . Since the exchange coupling J_{ex} is reduced with increasing U , the disturbance of the spin background costs less energy, and the spin-charge coupling becomes weaker. Hence, the U dependence of the HHG increase ratio suggests that the temperature dependence of HHG is related to the spin-charge coupling.

Subcycle analysis and dephasing. To further elucidate the origin of the temperature dependence, we perform a subcycle analysis of the HHG signal. Specifically, we consider a windowed Fourier transform $J(\omega, t_p) = \int dt e^{i\omega t} F_{\text{window}}(t - t_p) J(t)$ and evaluate $I_{\text{HHG}}(\omega, t_p) \equiv |\omega J(\omega, t_p)|^2$. The latter function provides the time-resolved spectral features of the emitted light around t_p . Since HHG in Mott insulators mainly originates from the recombination of doublon-holon pairs,^{26,30} the subcycle

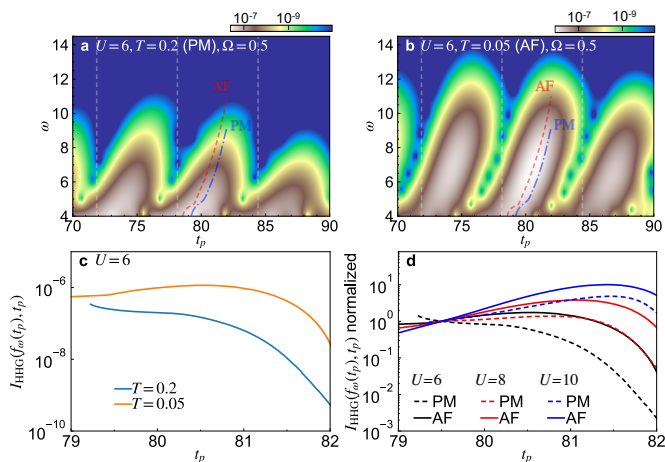


FIG. 4. **Subcycle features of the HHG signal of the Mott insulator.** **a,b** Subcycle spectra $I_{\text{HHG}}(\omega, t_p)$ for $U = 6$ at **a** $T = 0.2$ (PM phase) and at **b** $T = 0.05$ (AF phase). For the window Fourier transformation, we employ a Gaussian window whose standard deviation is $\sigma' = 0.9$. The red dashed (blue dot-dashed) lines indicate the maxima of $I_{\text{HHG}}(\omega, t_p)$ at $T = 0.05$ ($T = 0.2$) at a given ω as a function of t_p around $t_p = 80$, and represent the typical kinetics of doublon-holon pairs. These curves define the function $f_\omega(t_p)$. The vertical dashed lines indicate the times when the electric field $E(t) = 0$. **c** Intensity $I_{\text{HHG}}(\omega, t_p)$ along the lines $f_\omega(t_p)$ for $U = 6$. **d** Normalized intensity $I_{\text{HHG}}(\omega, t_p)$ along the lines $f_\omega(t_p)$ for the indicated values of U . We use $T = 0.2$ for the PM phase, while we use $T = 0.3/U$ for the AF states to take account of the change of $J_{\text{ex}} \propto \frac{1}{U}$. $I_{\text{HHG}}(f_\omega(t_p), t_p)$ is renormalized by the value at $t_p = 79.5$ in each case. The excitation parameters are $E_0 = 0.8$, $\Omega = 0.5$, $t_0 = 75$ and $\sigma = 15$.

spectra reveal the recombination time of the pairs and their energy at that time. In Figs. 4 **a,b**, we show the subcycle spectra in the PM and AF phases. In both cases, the dominant intensity appears at early times within one period, which suggests that only short trajectories of the doublon-holon pairs contribute to the HHG signal. In other words, the coherence time of the doublon-holon pair is very short ($< T_p/4$) compared to one cycle of the pulse field and to the coherence times typically considered in the analysis of semiconductors, see e.g. Fig. 6 in Ref. 12. The kinematics estimated from the peak position of $I_{\text{HHG}}(\omega, t_p)$ at each ω as a function of t_p is represented with red dashed (blue dot-dashed) lines for the AF (PM) phase in Figs. 4 **a,b**. These lines define the function $f_\omega(t_p)$. The difference between the blue and red lines is mostly explained by the difference in the gap size ($\simeq 1.1$), which indicates that the trajectory of the doublon-holon pair is almost the same in the AF and PM phases. The main difference is the coherence time of the pair.

To quantify this, in Fig. 4 **c**, we show the intensity along the peaks, $I_{\text{HHG}}(f_\omega(t_p), t_p)$. The results indeed show that for the higher temperature the intensity decays faster, which suggests that the dephasing time of the doublon-holon pair is shorter. This is in a stark contrast with the behavior of the charge distribution, where the

absence of the AF spin background at high temperature leads to a slower relaxation^{38–40}. On the other hand, with increasing U , the behavior of $I_{\text{HHG}}(f_\omega(t_p), t_p)$ in the AF and PM phases becomes more similar, see Fig. 4 **d**. Furthermore, the peak in $I_{\text{HHG}}(f_\omega(t_p), t_p)$ becomes clearer, which indicates that the intensity coming from longer-time trajectories of the doublon-holon pairs and hence the coherence time are increased. This feature appears counter-intuitive, because the single-particle spectrum becomes highly incoherent for large U ^{35,37}, and demonstrates that HHG in SCSs is not directly related to the single-particle spectra, in contrast to semiconductors, as already pointed out in previous works^{26,28,30}.

Role of the spin-charge coupling. We now argue that these behaviors can be consistently explained in terms of the spin-charge coupling. To directly compare cases with and without spin-charge coupling, we switch to the one-dimensional Hubbard model and apply a staggered magnetic field B_{stagg}^z . In one dimension, without B_{stagg}^z , the kinematics of the doublons and holons is independent of the spin-degrees of freedom (spin-charge separation), while for $B_{\text{stagg}}^z \neq 0$, the hopping of a doublon (holon) creates a mismatch between the staggered field and the spin configuration, as it happens in higher-dimensional systems without field, compare Fig. 5 **a** and Fig. 2 **c**. In other words, B_{stagg}^z plays the role of the mean fields of the magnetization from the neighboring sites perpendicular to the chain, and with this set-up, the one-dimensional model can mimic the spin-charge coupling in higher dimensions. The infinite time-evolving block decimation (iTEBD)⁴¹ allows to compute accurate results for this one-dimensional model at $T = 0$ in the thermodynamic limit (see Methods).

We show the HHG spectra for various B_{stagg}^z in Fig. 5 **b** and the corresponding subcycle analysis in Figs. 5 **c,d**. For small B_{stagg}^z , the expected HHG peaks at $(2n+1)\Omega$ in $I_{\text{HHG}}(\omega)$ are not clear, which suggests that the system is not fully time periodic during the pulse. This can be attributed to the long coherence time of the doublon-holon pair, which leads to interference of many quasi-classical trajectories within the three-step model¹². Indeed, the subcycle spectra for small B_{stagg}^z suggest that long trajectories of doublon-holon pairs strongly contribute to the HHG signal, see Fig. 5 **c**³⁰. With increasing B_{stagg}^z , the HHG intensity becomes weaker but the HHG peaks become clearer at $(2n+1)\Omega$. Here, B_{stagg}^z is chosen to be comparable to J_{ex} . In the subcycle spectrum, the weight is shifted to earlier times in one period, see Fig. 5 **d**, as it is the case in the DMFT results in Fig. 4 **b** at low temperatures. These results show that the coherence time of the doublon-holon pair is efficiently suppressed by the spin-charge coupling, which consistently explains the behavior of the DMFT results. The short coherence time reduces the interference between different quasi-classical trajectories and results in clear HHG peaks both in the DMFT data and the iTEBD data for nonzero B_{stagg}^z .

The reduction of the coherence time of the doublon-holon pair with increasing temperature can be under-

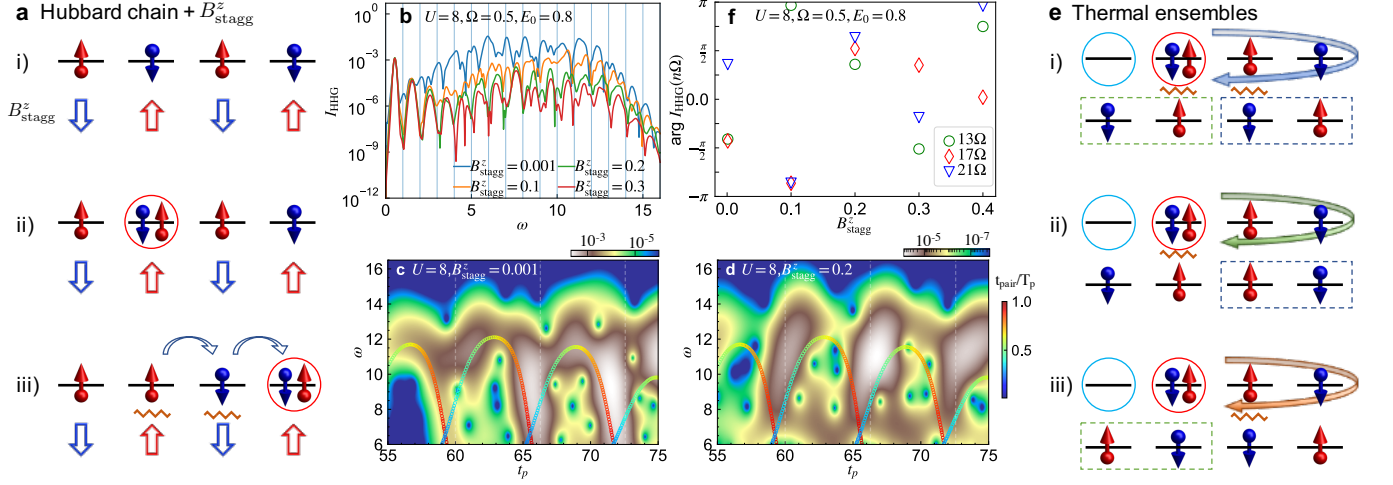


FIG. 5. **Effects of spin-charge coupling on HHG.** **a** Schematic pictures of the effects of the staggered magnetic field B_{stagg}^z applied to the one-dimensional Hubbard chain, which can be directly compared to Fig. 2 **c**. i) In equilibrium, each site is occupied by one electron, and the spin is aligned anti-parallel to the staggered field. ii), iii) As the doublon moves, it produces a mismatch between the spin configuration and the staggered magnetic field at the cost of the Zeeman energy, about B_{stagg}^z (zigzag lines). **b** The HHG spectrum for the one-dimensional Hubbard model evaluated with iTEBD. **c,d** The corresponding subcycle analysis for $B_{\text{stagg}}^z = 0.001$ (**c**) and $B_{\text{stagg}}^z = 0.2$ (**d**). For the window Fourier transformation, we employ a Gaussian window whose standard deviation is $\sigma' = 0.9$. The colored markers indicate the energy emitted at t_p by the recombination of a doublon-holon pair, which is predicted from the three-step model using the doublon and holon dispersions from the Bethe ansatz following Ref. 30. The color indicates the time interval between the recombination and the creation of the doublon-holon pair t_{pair} , and $T_p = \frac{2\pi}{\Omega}$. **e** Schematic pictures of the interplay between thermal ensembles and spin-charge coupling. Panels i)-iii) show cases with different spin configurations activated by thermal fluctuations. The difference between case i) and case ii) is indicated by the blue dashed rectangle, while that between case i) and case iii) is indicated by the green dashed rectangle. The zigzag lines in each panel show the sites where the mismatch in the spin configuration occurs as the doublon moves around. The horizontal arrows with different colors indicate the difference in the kinematics of the doublon due to the spin-charge coupling. **f** The phase of the Fourier component of the current $J(\omega)$ at $\omega = n\Omega$ (n is an integer). For **b-d** and **f**, we set $U = 8$, and the excitation parameters are $\Omega = 0.5$, $E_0 = 0.8$, $t_0 = 60$ and $\sigma = 15$.

stood as a cooperative effect of the spin-charge coupling and the thermal ensemble. At nonzero temperatures, the initial equilibrium state is described by an ensemble of eigenstates, represented by the density matrix $\hat{\rho} = e^{-\beta\hat{H}}/Z$ with $Z = \text{Tr}[e^{-\beta\hat{H}}]$. In such a system, the total current induced by the field can be calculated as the ensemble average over the individual currents evaluated for these eigenstates. With increasing temperature, the weight of the high-energy states increases. In our case, at higher temperatures, spin configurations different from the AF ground state are activated, see Fig. 5 **e**. The dynamics of the doublon or holon is different for each configuration, since the energy transfer to the spin background during an excursion depends on the spin configuration. This should produce emitted light waves with different phases for different spin configurations, resulting in phase cancellations after the ensemble average, and thus reduce the coherence between the doublon-holon pairs with increasing temperature. Note that this effect does not rely on long-range magnetic ordering and is also relevant in the PM phase. This effect is similar to the effect of disorder in semiconductors, which reduces the coherence of electron-hole pairs⁴². However, a crucial difference is that the effect investigated here is activated

by temperature in SCSs and absent without spin-charge coupling. Namely, for small J_{ex} , weaker cancellations between different spin configurations are expected, which is consistent with the results in Fig. 4 **d**, and explains the reduction of the enhancement of the HHG signal with larger U in Fig. 3 **c**. To exemplify that the spin-charge coupling can indeed provide such phase shifts, in Fig. 5 **f**, we show the B_{stagg}^z -dependence of the phase of $J(\omega)$ for $\omega = n\Omega$ (with n some integer). The result suggests that the phase is sensitive to B_{stagg}^z , which supports the above argument. Thus, we conclude that, in the present system, the modification of the coherence time due to the spin-charge coupling and thermal fluctuations dominates over the reduction of the tunneling rate by the gap opening, leading to an enhancement of the HHG intensity at lower temperatures.

Discussion

The strong temperature dependence of the HHG spectrum observed in Mott insulators is not expected in typical semiconductors. In the theoretical analysis of HHG in semiconductors, one often assumes a short dephasing time T_2 of a few fs for an electron-hole pair. However, the origin of this short dephasing time is distinct from that in Mott insulators. One relevant factor is the experimental

setup, i.e. the dephasing by the propagation of light and the inhomogeneity of the field strength^{18,43}. However, this should be insensitive to temperature. The other major factor is the electron-electron scattering among excited carriers in semiconductors^{44,45}. For example, a dephasing time of the order of ten fs has been reported in GaAs, and strongly depends on the number of injected carriers⁴⁴. This mechanism is also expected to be insensitive to temperature, since thermal fluctuations cannot efficiently excite carriers across the gap. These considerations are supported by the experimental HHG spectrum for the semiconductor InAs, which is insensitive to temperature, as shown by the open symbols in Fig. 1 a. Furthermore, we note that $T_2 \geq \frac{T_p}{4}$ is often used for semiconductors, but even if T_2 varies with temperature in this range, the shape of the HHG spectrum and the cutoff frequency are hardly modulated¹¹.

Spin-charge coupling is inevitable in Mott insulators in dimensions larger than one, and thus the strong temperature dependence is expected to be a generic feature of HHG in SCSs. Indeed, our DMFT analysis qualitatively reproduces the characteristic enhancement of the HHG intensity in Ca_2RuO_4 ³³ (Fig. 1). We would like to point out, however, that Ca_2RuO_4 shows a strong temperature dependence even above T_c ($= 110$ K), unlike the DMFT result. This difference can be explained as follows. On the one hand, since the trajectories of the doublon-holon pairs are expected to be short, HHG should be sensitive to short-range AF order, which still exists above T_c . In the DMFT approximation, however, the effects of short-range spin order above T_c are not captured. On the other hand, in multi-orbital systems like Ca_2RuO_4 , the dynamics of the excited multiplets disturbs the orbital configurations and the resulting orbital-charge coupling plays a similar role as the spin-charge coupling⁴⁶. We expect that, in Ca_2RuO_4 , both of these effects contribute to the strong temperature dependence observed even above T_c .

In summary, our theoretical study revealed that the spin-charge coupling has a crucial effect on HHG in Mott insulators. Spin-charge coupling leads to short coherence times, even at low temperatures, and its cooperation with thermal fluctuations produces disorder-like effects which further reduce the coherence. As a result, the HHG spectrum of Mott insulators exhibits a strong temperature dependence. In particular, a counter-intuitive enhancement of the HHG intensity accompanied by a gap increase is observed when the temperature is lowered.

Our results provide a useful guidance for the future exploration of HHG in SCSs. Firstly, our results suggest that the temperature dependence of the HHG intensity can be controlled by changing the ratio $\frac{U}{t_{\text{hop}}}$, which is feasible with the application of chemical or physical pressure. Secondly, to realize a strong HHG signal, one-dimensional Mott systems are more favorable than higher-dimensional ones due to the absence of the spin-charge coupling. The recovery of coherence and the possible increase of the HHG intensity due to the reduction of the dimensionality could be systematically analyzed by

exploiting the dimensional crossover in ladder-type compounds such as $\text{Sr}_{n-1}\text{Cu}_{n+1}\text{O}_{2n}$ ³⁴. Furthermore, the sensitivity of HHG to the temperature and spin-charge coupling suggests possible HHG-based techniques for detecting and characterizing thermal and non-thermal phases, and for measuring the strength of the spin-charge coupling.

In this paper, we focused on the effects of the spin-charge coupling in the single-band Hubbard model. However, in more general SCSs, the interplay of spin, orbital and charge degrees of freedoms produces interesting many-body elemental excitations and multiplets. Furthermore, some SCSs can be described by the double-exchange model, which exhibits a different type of spin-charge coupling. How these many-body excitations and different spin-charge interactions affect the HHG mechanism in these systems should be clarified in view of novel applications of HHG spectroscopy in SCSs.

METHODS

Non-equilibrium dynamical mean-field theory.

The dynamical mean-field theory (DMFT) is a powerful theoretical framework that can deal with strongly correlated systems⁴⁷, in particular the Mott physics, and the nonequilibrium DMFT is its extension to nonequilibrium problems³⁶. In nonequilibrium DMFT, we map the lattice system to an effective impurity model with a self-consistently determined time-dependent noninteracting bath³⁶. In the present case, we consider the single-band Hubbard model with a possible AF order, and assume that the spins can be polarized along the z axis. In the AF phase, the two sublattices A and B show opposite magnetizations and effective impurity models are introduced for each sublattice. The action of the impurity model for the sublattice α can be expressed as

$$S_{\text{imp}}^{\alpha} = -i \int dt dt' \sum_{\sigma} \hat{d}_{\sigma}^{\dagger}(t) \Delta_{\sigma}^{\alpha}(t, t') \hat{d}_{\sigma}(t') - i \int dt \hat{H}_{\text{loc}}(t), \quad (2)$$

where Δ is the hybridization function and $\hat{H}_{\text{loc}}(t) = -\mu \sum_{\sigma} \hat{d}_{\sigma}^{\dagger}(t) \hat{d}_{\sigma}(t) + U \hat{d}_{\uparrow}^{\dagger}(t) \hat{d}_{\uparrow}(t) \hat{d}_{\downarrow}^{\dagger}(t) \hat{d}_{\downarrow}(t)$. In DMFT, Δ is self-consistently determined such that the local Green's functions and the self-energies of the lattice are the same as those of the impurity model. We solve the impurity model using the non-crossing approximation (NCA)⁴⁸, which yields reliable results in the strong coupling regime.

The lattice self-consistency condition for the hybridization function used in the main text is $\Delta_{\sigma}^{\alpha}(\nu, \nu') = \sum_{\xi=\pm} \Delta_{\sigma, \xi}^{\alpha}(\nu, \nu')$, where $\xi = \pm$ corresponds to the positive/negative bond direction (relative to the polarization of the field) and $\Delta_{\sigma, \pm}^{\alpha}(\nu, \nu') = \frac{t_{\text{hop}}^2}{2} e^{\pm iA(\nu)} G_{\text{imp}, \sigma}^{\bar{\alpha}}(\nu, \nu') e^{\mp iA(\nu')}$, with A the vector potential of the field pulse⁴⁹. Here, the bond length a and the electron charge are set to unity. The vector potential is related to the electric field $E(t)$ by $E(t) = -\partial_t A(t)$. We choose the vector potential

$A(t) = \frac{E_0}{\Omega} F_G(t, t_0, \sigma) \sin(\Omega(t - t_0))$ with $F_G(t, t_0, \sigma) = \exp[-\frac{(t-t_0)^2}{2\sigma^2}]$. E_0 indicates the maximum value of the electric field. The corresponding current (per site) can be computed as $J(t) = \text{Im}[\sum_{\sigma, \xi=\pm} \xi \Gamma_{\sigma, \xi}^\alpha(t)]$, where $\Gamma_{\sigma, \pm}^\alpha(t) \equiv -i[G_{\text{imp}, \sigma}^\alpha * \Delta_{\sigma, \pm}^\alpha]^\prec(t, t)$. The self-consistency condition represents a Bethe lattice with d bonds connected to each lattice site, where we take the limit of $d \rightarrow \infty$ with a rescaled hopping parameter t_{hop}/\sqrt{d} . In the free system ($U = 0$), the full bandwidth becomes $W = 4t_{\text{hop}}$. For the Bethe lattice, the self-consistency condition is simplified, compared to other lattices, which reduces the numerical cost and enables a systematic analysis. The qualitative features of the HHG spectrum are expected to be insensitive to the choice of the lattice. In SI, we confirm this point with simulations for the two-dimensional square lattice, although the scope of this analysis is limited.

In equilibrium, we define the momentum-averaged single-particle spectral function as

$$A_{\text{loc}}(\omega) = -\frac{1}{\pi} \text{Im} G_{\text{loc}}^R(\omega). \quad (3)$$

Here, we introduced the retarded Green's function $G_{ij, \sigma}^R(t - t') = -i\theta(t - t')\{\hat{c}_{i\sigma}(t)\hat{c}_{j\sigma}^\dagger(t')\}$, and $G_{\text{loc}} = \frac{1}{N} \sum_i G_{ii, \sigma}$. $G^R(\omega)$ is defined as $\int dt e^{i\omega t} G^R(t)$. In practice, since the simulation is limited to finite t , we use a Gaussian window function with standard deviation $\sigma' = 8$ in the Fourier transformation. The Mott gap Δ_{Mott} is determined by the criterion $A_{\text{loc}}(\Delta_{\text{Mott}}/2) = \delta$ with $\delta = 0.005$. We checked that the choice of δ has no qualitative effect on the results.

Infinite time-evolving block decimation. The Hamiltonian of the one-dimensional Hubbard model considered here is

$$\hat{H}(t) = -t_{\text{hop}} \sum_{i, \sigma} [e^{-iA(t)} \hat{c}_{i, \sigma}^\dagger \hat{c}_{i+1, \sigma} + h.c.] \quad (4)$$

$$+ U \sum_i \hat{n}_{i, \uparrow} \hat{n}_{i, \downarrow} + B_{\text{stag}}^z \sum_i (-1)^i \hat{S}_{z, i},$$

where $\hat{S}_{z, i} = \frac{1}{2}(\hat{n}_{i, \uparrow} - \hat{n}_{i, \downarrow})$ and t_{hop} is set to unity. We an-

alyze this model with the infinite time-evolving block decimation (iTEBD) method⁴¹. In iTEBD, assuming translational invariance, we express the wave function of the system as a matrix product state (MPS). iTEBD directly treats the thermodynamic limit and we use the cut-off dimension $D = 2000$ for the MPS to obtain converged results. In the implementation, we use the conservation laws for the numbers of spin-up and spin-down electrons to improve the numerical efficiency.

Data availability

The data that support the findings of this study are available from the corresponding author upon reasonable request.

Code availability

The DMFT part is based on the open source library Nessi⁵⁰. The specific code for the calculations performed in this work is available from the corresponding authors upon reasonable request.

Acknowledgements

The calculations have been performed on the Beo05 cluster at the University of Fribourg. This work is supported by Grant-in-Aid for Scientific Research from JSPS, KAKENHI Grant Nos. JP20K14412(Y.M.), JP21H05017(Y.M., K.U., K.T.), JP19H05821, JP18K04678, JP17K05536 (A.K.), JST CREST Grant No. JPMJCR1901 (Y.M.), and ERC Consolidator Grant No. 724103 (P.W.).

Authors contributions

Y. M. conceived the project. P. W., K. T. and A. K. supervised the project. Y. M. made all the numerical simulations. K. U. and the other co-authors contributed to the discussions and the writing of the manuscript.

Competing interests

The authors declare no competing interests.

Additional information

Supplementary Information accompanies this paper at [link to be added].

¹ M. Ferray, A. L'Huillier, X. F. Li, L. A. Lompre, G. Mainfray, and C. Manus, *Journal of Physics B: Atomic, Molecular and Optical Physics* **21**, L31 (1988).

² F. Krausz and M. Ivanov, *Rev. Mod. Phys.* **81**, 163 (2009).

³ S. Ghimire, A. D. DiChiara, E. Sistrunk, P. Agostini, L. F. DiMauro, and D. A. Reis, *Nat. Phys.* **7**, 138 (2011).

⁴ O. Schubert, M. Hohenleutner, F. Langer, B. Urbank, C. Lange, U. Huttner, D. Golde, T. Meier, M. Kira, S. W. Koch, and R. Huber, *Nat. Photon.* **8**, 119 (2014).

⁵ T. T. Luu, M. Garg, S. Y. Kruchinin, A. Moulet, M. T. Hassan, and E. Goulielmakis, *Nature (London)* **521**, 498 (2015).

⁶ F. Langer, M. Hohenleutner, C. P. Schmid, C. Pöllmann,

P. Nagler, T. Korn, C. Schüller, M. Sherwin, U. Huttner, J. Steiner, S. Koch, M. Kira, and R. Huber, *Nature (London)* **533**, 225 (2016).

⁷ G. Ndabashimiye, S. Ghimire, M. Wu, D. A. Browne, K. J. Schafer, M. B. Gaarde, and D. A. Reis, *Nature (London)* **534**, 520 (2016).

⁸ Y. S. You, D. A. Reis, and S. Ghimire, *Nat. Phys.* **13**, 345 (2017).

⁹ N. Yoshikawa, T. Tamaya, and K. Tanaka, *Science* **356**, 736 (2017).

¹⁰ H. A. Hafez, S. Kovalev, J.-C. Deinert, Z. Mics, B. Green, N. Awari, M. Chen, S. Germanskiy, U. Lehnert, J. Teichert, Z. Wang, K.-J. Tielrooij, Z. Liu, Z. Chen, A. Narita,

- K. Mullen, M. Bonn, M. Gensch, and D. Turchinovich, *Nature (London)* **561**, 507 (2018).
- ¹¹ G. Vampa, C. R. McDonald, G. Orlando, D. D. Klug, P. B. Corkum, and T. Brabec, *Phys. Rev. Lett.* **113**, 073901 (2014).
- ¹² G. Vampa, C. R. McDonald, G. Orlando, P. B. Corkum, and T. Brabec, *Phys. Rev. B* **91**, 064302 (2015).
- ¹³ M. Wu, S. Ghimire, D. A. Reis, K. J. Schafer, and M. B. Gaarde, *Phys. Rev. A* **91**, 043839 (2015).
- ¹⁴ T. Ikemachi, Y. Shinohara, T. Sato, J. Yumoto, M. Kuwata-Gonokami, and K. L. Ishikawa, *Phys. Rev. A* **95**, 043416 (2017).
- ¹⁵ K. K. Hansen, T. Deffge, and D. Bauer, *Phys. Rev. A* **96**, 053418 (2017).
- ¹⁶ N. Tancogne-Dejean, O. D. Mücke, F. X. Kärtner, and A. Rubio, *Nat. Comm.* **8**, 745 (2017).
- ¹⁷ E. N. Osika, A. Chacón, L. Ortmann, N. Suárez, J. A. Pérez-Hernández, B. Szafran, M. F. Ciappina, F. Sols, A. S. Landsman, and M. Lewenstein, *Phys. Rev. X* **7**, 021017 (2017).
- ¹⁸ I. Floss, C. Lemell, G. Wachter, V. Smejkal, S. A. Sato, X.-M. Tong, K. Yabana, and J. Burgdörfer, *Phys. Rev. A* **97**, 011401 (2018).
- ¹⁹ G. Vampa, T. J. Hammond, N. Thiré, B. E. Schmidt, F. Légaré, C. R. McDonald, T. Brabec, D. D. Klug, and P. B. Corkum, *Phys. Rev. Lett.* **115**, 193603 (2015).
- ²⁰ T. T. Luu and H. J. Wörner, *Nat. Comm.* **9**, 916 (2018).
- ²¹ K. Uchida, V. Pareek, K. Nagai, K. M. Dani, and K. Tanaka, *Phys. Rev. B* **103**, L161406 (2021).
- ²² A. F. Kemper, B. Moritz, J. K. Freericks, and T. P. Devereaux, *New J. Phys.* **15**, 023003 (2013).
- ²³ S. Y. Kruchinin, F. Krausz, and V. S. Yakovlev, *Rev. Mod. Phys.* **90**, 021002 (2018).
- ²⁴ S. Ghimire and D. A. Reis, *Nat. Phys.* **15**, 10 (2019).
- ²⁵ R. E. F. Silva, I. V. Blinov, A. N. Rubtsov, O. Smirnova, and M. Ivanov, *Nat. Photon.* **12**, 266 (2018).
- ²⁶ Y. Murakami, M. Eckstein, and P. Werner, *Phys. Rev. Lett.* **121**, 057405 (2018).
- ²⁷ N. Tancogne-Dejean, M. A. Sentef, and A. Rubio, *Phys. Rev. Lett.* **121**, 097402 (2018).
- ²⁸ S. Imai, A. Ono, and S. Ishihara, *Phys. Rev. Lett.* **124**, 157404 (2020).
- ²⁹ C. Orthodoxou, A. Zair, and G. H. Booth, *npj Quantum Materials* **6**, 76 (2021).
- ³⁰ Y. Murakami, S. Takayoshi, A. Koga, and P. Werner, *Phys. Rev. B* **103**, 035110 (2021).
- ³¹ O. Grånäs, I. Vaskivskyi, P. Thunström, S. Ghimire, R. Knut, J. Söderström, L. Kjellsson, D. Turenne, R. Y. Engel, M. Beye, J. Lu, A. H. Reid, W. Schlotter, G. Coslovich, M. Hoffmann, G. Kolesov, C. Schüßler-Langeheine, A. Styervoyedov, N. Tancogne-Dejean, M. A. Sentef, D. A. Reis, A. Rubio, S. S. P. Parkin, O. Karis, J. Nordgren, J. E. Rubensson, O. Eriksson, and H. A. Dürr, *arXiv:2008.11115* (2020).
- ³² M. R. Bionta, E. Haddad, A. Leblanc, V. Gruson, P. Lassonde, H. Ibrahim, J. Chaillou, N. Émond, M. R. Otto, A. Jiménez-Galán, R. E. F. Silva, M. Ivanov, B. J. Siwick, M. Chaker, and F. m. c. Légaré, *Phys. Rev. Research* **3**, 023250 (2021).
- ³³ K. Uchida, G. Mattoni, S. Yonezawa, F. Nakamura, Y. Maeno, and K. Tanaka, “High-order harmonic generation and its unconventional scaling law in the mott-insulating Ca_2RuO_4 ,” (2021), *arXiv:2106.15478* [PRL accepted].
- ³⁴ M. Imada, A. Fujimori, and Y. Tokura, *Rev. Mod. Phys.* **70**, 1039 (1998).
- ³⁵ E. Dagotto, *Rev. Mod. Phys.* **66**, 763 (1994).
- ³⁶ H. Aoki, N. Tsuji, M. Eckstein, M. Kollar, T. Oka, and P. Werner, *Rev. Mod. Phys.* **86**, 779 (2014).
- ³⁷ G. Sangiovanni, A. Toschi, E. Koch, K. Held, M. Capone, C. Castellani, O. Gunnarsson, S.-K. Mo, J. W. Allen, H.-D. Kim, A. Sekiyama, A. Yamasaki, S. Suga, and P. Metcalf, *Phys. Rev. B* **73**, 205121 (2006).
- ³⁸ Z. Lenarčič and P. Prelovšek, *Phys. Rev. Lett.* **111**, 016401 (2013).
- ³⁹ D. Golež, J. Bonča, M. Mierzejewski, and L. Vidmar, *Phys. Rev. B* **89**, 165118 (2014).
- ⁴⁰ M. Eckstein and P. Werner, *Scientific Reports* **6**, 21235 (2016).
- ⁴¹ G. Vidal, *Phys. Rev. Lett.* **91**, 147902 (2003).
- ⁴² G. Orlando, C.-M. Wang, T.-S. Ho, and S.-I. Chu, *J. Opt. Soc. Am. B* **35**, 680 (2018).
- ⁴³ I. Kilen, M. Kolesik, J. Hader, J. V. Moloney, U. Huttner, M. K. Hagen, and S. W. Koch, *Phys. Rev. Lett.* **125**, 083901 (2020).
- ⁴⁴ P. C. Becker, H. L. Fragnito, C. H. B. Cruz, R. L. Fork, J. E. Cunningham, J. E. Henry, and C. V. Shank, *Phys. Rev. Lett.* **61**, 1647 (1988).
- ⁴⁵ K. Nagai, K. Uchida, S. Kusaba, T. Endo, Y. Miyata, and K. Tanaka, “Effect of incoherent electron-hole pairs on high harmonic generation in atomically thin semiconductors,” (2021), *arXiv:2112.12951* [physics.optics].
- ⁴⁶ H. U. R. Strand, D. Golež, M. Eckstein, and P. Werner, *Phys. Rev. B* **96**, 165104 (2017).
- ⁴⁷ A. Georges, G. Kotliar, W. Krauth, and M. J. Rozenberg, *Rev. Mod. Phys.* **68**, 13 (1996).
- ⁴⁸ M. Eckstein and P. Werner, *Phys. Rev. B* **82**, 115115 (2010).
- ⁴⁹ P. Werner, H. U. R. Strand, S. Hoshino, and M. Eckstein, *Phys. Rev. B* **95**, 195405 (2017).
- ⁵⁰ M. Schüler, D. Golež, Y. Murakami, N. Bittner, A. Herrmann, H. U. Strand, P. Werner, and M. Eckstein, *Computer Physics Communications* **257**, 107484 (2020).

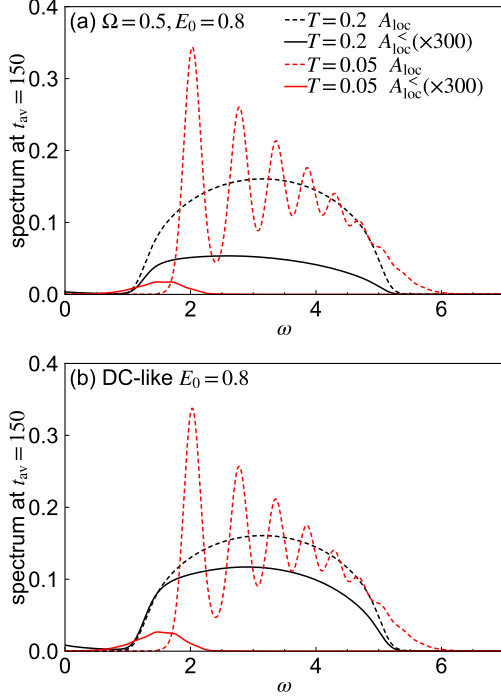


FIG. 6. Single-particle spectral functions $A_{\text{loc}}(\omega, t_{\text{av}})$ and $A_{\text{loc}}^<(\omega, t_{\text{av}})$ after the application of the electric field. $A_{\text{loc}}^<(\omega, t_{\text{av}})$ measures the density of carriers excited by the field. We set $U = 6$ and the pulse parameters are (a) $\Omega = 0.5, E_0 = 0.8, t_0 = 75$ and $\sigma = 15$, and (b) $E_0 = 0.8, t_0 = 75$ and $\sigma = 15$. In all cases, we take $t_{\text{av}} = 150$.

Appendix A: Additional results for the Bethe lattice

In this section, we present supplementary results obtained with DMFT for the Hubbard model on the Bethe lattice. First, we show the temperature dependence of the number of charge carriers created by the field. To this end, we compute the time-dependent single-particle spectral functions³⁶

$$\begin{aligned} A_{\text{loc}}(\omega, t_{\text{av}}) &= -\frac{1}{\pi} \text{Im} G_{\text{loc}}^R(\omega, t_{\text{av}}), \\ A_{\text{loc}}^<(\omega, t_{\text{av}}) &= \frac{1}{2\pi} \text{Im} G_{\text{loc}}^<(\omega, t_{\text{av}}). \end{aligned} \quad (\text{A1})$$

Here, we introduced the Green's functions $G_{ij,\sigma}(t, t') = -i\langle T_C \hat{c}_{i\sigma}(t) \hat{c}_{j\sigma}^\dagger(t') \rangle$ with T_C being the contour ordering operator, $G_{\text{loc}} = \frac{1}{N} \sum_i G_{ii,\sigma}$, and G^R and $G^<$ are the retarded and lesser parts of the Green's function. $G^{R/<}(\omega, t_{\text{av}})$ is defined as $\int dt_{\text{rel}} e^{i\omega t_{\text{rel}}} G^{R/<}(t_{\text{rel}}, t_{\text{av}})$, where $G^{R/<}(t_{\text{rel}}, t_{\text{av}}) = G^{R/<}(t, t')$, $t_{\text{rel}} = t - t'$ and $t_{\text{av}} = \frac{t+t'}{2}$. $A_{\text{loc}}(\omega, t_{\text{av}})$ yields the energy spectrum at time t_{av} and $A_{\text{loc}}^<(\omega, t_{\text{av}})$ the occupied states. Figure S6 shows how many charge carriers are created after the pulse field. Panel (a) plots the results for the same condition as in the main text, while panel (b) shows the results

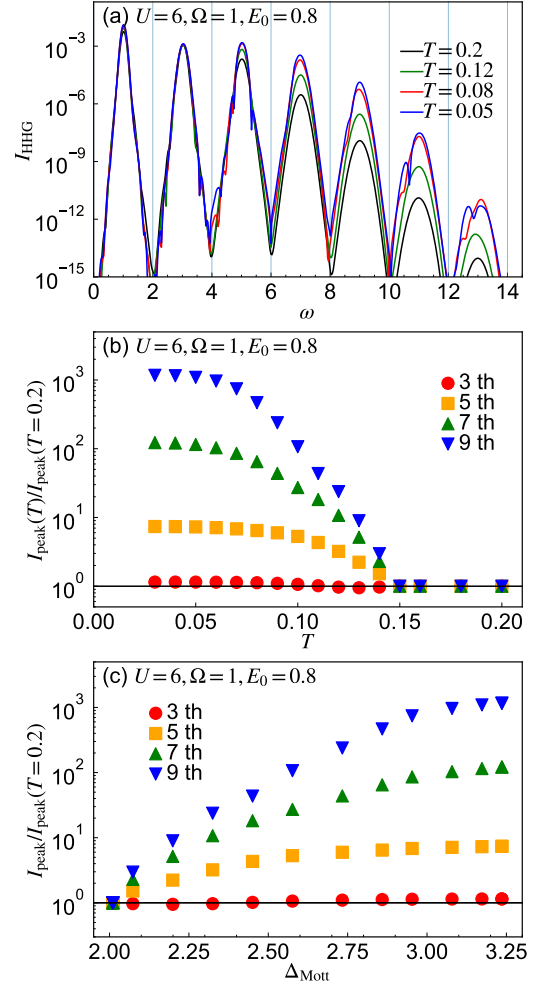


FIG. 7. (a) HHG spectra $I_{\text{HHG}}(\omega)$ of the Mott insulator evaluated with DMFT for various temperatures. (b) The intensity at the peaks of the HHG spectra I_{peak} as a function of the temperature. (c) The intensity at the peaks of the HHG spectra as a function of the Mott gap size Δ_{Mott} . In panels (b) and (c), the peak intensity is normalized by the value at $T = 0.2$. Here, we set $U = 6$ and consider the Bethe lattice. The pulse parameters are $\Omega = 1, E_0 = 0.8, t_0 = 75$ and $\sigma = 15$.

for a pulse without oscillations ($E(t) = E_0 F_G(t, t_0, \sigma)$), i.e. close to a DC excitation. Both panels demonstrate that a much smaller amount of charge carriers is produced when the temperature is lowered and the Mott gap is increased, as expected.

Next, we show the supplemental data for the HHG spectra for $\Omega = 1$. This excitation frequency is twice larger than what is used in the main text, and, in terms of the value of $\Delta_{\text{Mott}}/\Omega$, this choice is closer to the situation in the experiments on Ca_2RuO_4 ³³. In Fig. S7 (a), we show the HHG spectra for $U = 6$ for different temperatures. The corresponding temperature dependence of the intensity of the HHG peaks is shown in Fig. S7 (b), while the HHG peak intensity is shown as a function of the Mott gap in Fig. S7 (c). The intensity of the n th HHG

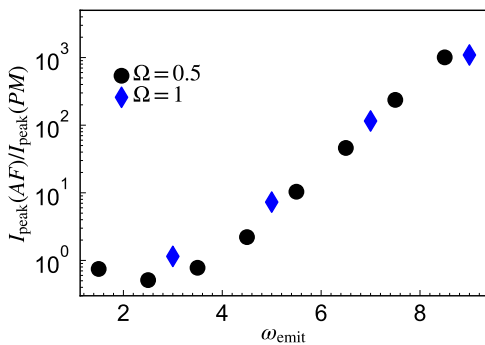


FIG. 8. The increase ratio of the HHG peak intensity, $I_{\text{peak}}(\text{AF})/I_{\text{peak}}(\text{PM})$, for the n th harmonics as a function of the emitted energy $\omega_{\text{emit}} = n\Omega$. Here, we set $U = 6$ and consider the Bethe lattice. The pulse parameters are $E_0 = 0.8$, $t_0 = 75$ and $\sigma = 15$.

peak I_{peak} is defined as the maximum value of $I_{\text{HHG}}(\omega)$ for $\omega \in [(n-1)\Omega, (n+1)\Omega]$. Since now the gap size is two to three times the excitation frequency, one may expect that multi-photon excitation processes play an important role. Still, the results shown in Fig. S7 indicate that the qualitative temperature dependence of the HHG spectrum is qualitatively the same as that for $\Omega = 0.5$ and that the characteristic increase of the HHG intensity with decreasing temperature is insensitive to the excitation condition. Furthermore, the match between the experiment for Ca_2RuO_4 and the theory is better for $\Omega = 1$ than for $\Omega = 0.5$, compare Fig. S7(c) with Fig. 1 in the main text.

In addition, we observe that the increase ratio of the HHG peak intensity is essentially determined by the emission photon energy. In Fig. S8, we show the increase ratio $I_{\text{peak}}(\text{AF})/I_{\text{peak}}(\text{PM})$ for the n th harmonics as a function of the emitted energy $\omega_{\text{emit}} = n\Omega$. The qualitatively same behavior has also been found in the experiments on Ca_2RuO_4 ³³.

Appendix B: Results for the square lattice

In this section, we present supplementary DMFT results for the Hubbard model on the two-dimensional square lattice at half filling. We show that the equilibrium features and the characteristic temperature dependence of the HHG are essentially the same as in the case of the Bethe lattice, although a systematic analysis is difficult since the DMFT calculation becomes numerically more demanding. We assume that the system only has nearest neighbor hopping, t_{hop} . We set $t_{\text{hop}} = 0.5$ so that the bandwidth of the free system becomes 4 as in the case of the Bethe lattice. The lattice constant a is set unity. In the following the system size is $(L_x, L_y) = (16, 16)$, where L_x (L_y) is the number of sites along the x (y) axis, and we use periodic boundary conditions.

In Fig. S9, we show the local single-particle spectral function $A_{\text{loc}}(\omega)$ and the momentum-resolved single-

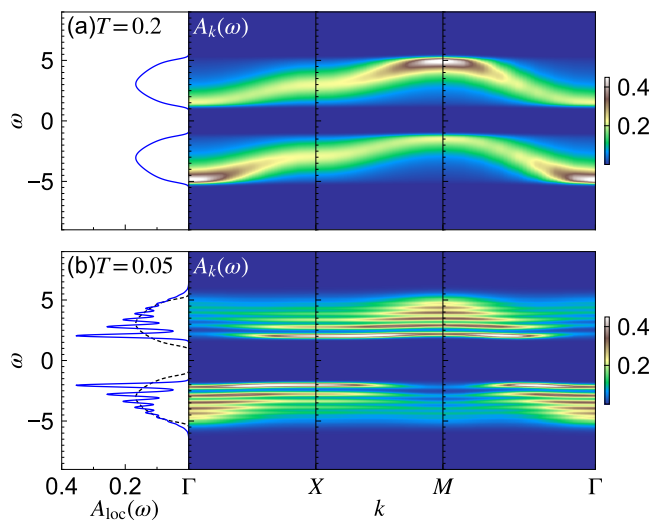


FIG. 9. Local single-particle spectral functions $A_{\text{loc}}(\omega)$ and momentum-resolved single-particle spectral functions $A_{\mathbf{k}}(\omega)$ for the Hubbard model on the two-dimensional square lattice. Panel (a) is for $T = 0.2$ in the PM phase and (b) is for $T = 0.05$ in the AF phase. Here, $U = 6$, $t_{\text{hop}} = 0.5$ and $(L_x, L_y) = (16, 16)$. In the momentum-resolved spectra, Γ , X and M follow the canonical notation for the Brillouin zone of the PM phase.

particle spectral function $A_{\mathbf{k}}(\omega)$ in equilibrium. The latter is defined as $A_{\mathbf{k}}(\omega) = -\frac{1}{\pi} \text{Im} G_{\mathbf{k},\sigma}^R(\omega)$, where $G_{\mathbf{k},\sigma}^R(\omega)$ is the Fourier component of the retarded part of the Green's function $G_{\mathbf{k},\sigma}(t)$. Here, $G_{\mathbf{k},\sigma}(t) = -i \langle T_C \hat{c}_{\mathbf{k}\sigma}(t) \hat{c}_{\mathbf{k}\sigma}^\dagger(0) \rangle$ and $\hat{c}_{\mathbf{k}\sigma}^\dagger = \frac{1}{\sqrt{N}} \sum_l e^{i\mathbf{k}\cdot\mathbf{r}_l} \hat{c}_{l\sigma}^\dagger$. As in the case of the Bethe lattice, the local spectral function $A_{\text{loc}}(\omega)$ is featureless above the transition temperature T_c . Below T_c the Mott gap is enhanced and peaks corresponding to spin polarons emerge. In the PM phase, the dispersions of the upper and lower Hubbard bands are parallel to each other, similar to the prediction of the Hubbard I approximation, see Fig. S9(a). On the other hand, in the AF phase, the momentum-resolved spectral function consists of many almost-flat spin-polaron bands, see Fig. S9(b). Also, at each momentum, the spectral function covers a wider frequency range than in the PM phase, and as a whole the dispersion relation is less well-defined than in the PM phase, i.e. the spectra look more incoherent. Based on the experience from HHG in semiconductors, these observations lead to the natural expectation that the HHG intensity should decrease with decreasing temperature.

Next, we discuss the HHG spectrum of this system. We apply linearly polarized light along the $\mathbf{e}_\theta = [\cos(\theta), \sin(\theta)]$ direction:

$$A_x(t) = \frac{E_0}{\Omega} \cos(\theta) F_G(t, t_0, \sigma) \sin(\Omega(t - t_0)), \quad (\text{B1})$$

$$A_y(t) = \frac{E_0}{\Omega} \sin(\theta) F_G(t, t_0, \sigma) \sin(\Omega(t - t_0)). \quad (\text{B2})$$

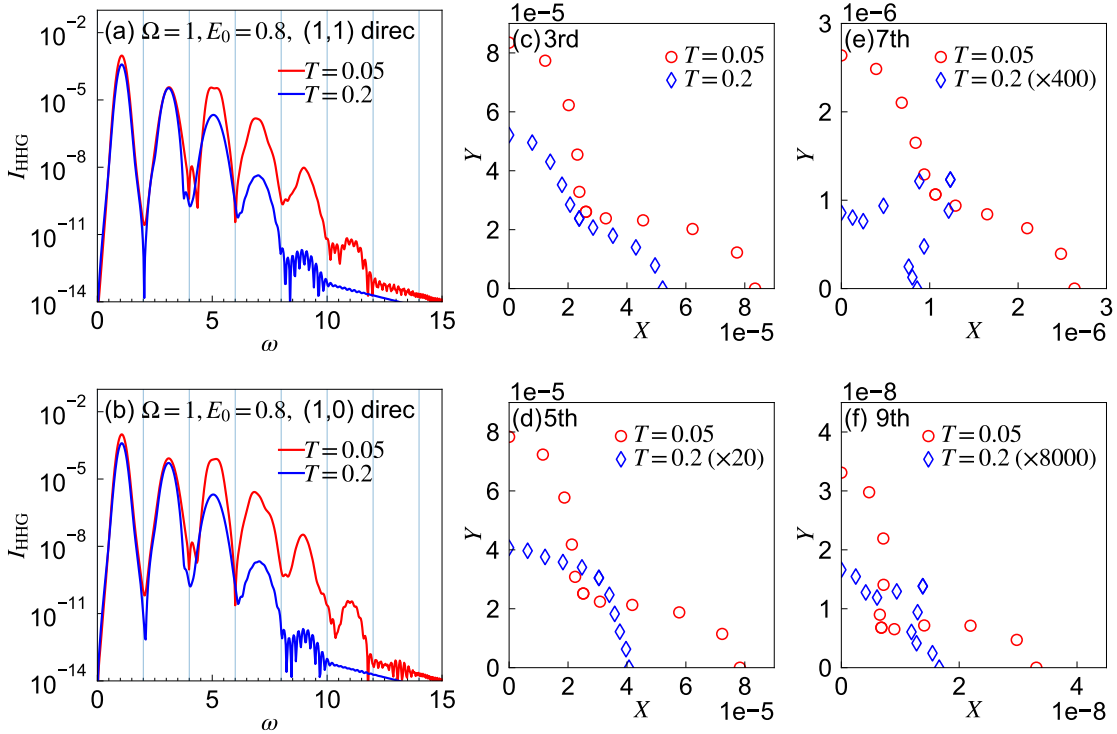


FIG. 10. (a)(b) HHG spectra of the Mott insulator evaluated with DMFT for the indicated temperatures. Here, we consider the Hubbard model on the two-dimensional square lattice and set $U = 6$ and $t_{\text{hop}} = 0.5$. The pulse parameters are (a) $\Omega = 1, E_0 = 0.8, t_0 = 30, \sigma = 7.5$ and $\theta = 0$, and (b) $\Omega = 1, E_0 = 0.8, t_0 = 30, \sigma = 7.5$ and $\theta = \pi/4$. (c-f) The corresponding polarization dependence of the HHG peak intensity. In all cases, we evaluate the HHG intensity along the direction of the applied electric field.

We extract the HHG signal along the \mathbf{e}_θ direction from the Fourier transformation of $J_\theta(t)$, where $J_\theta(t) = \mathbf{e}_\theta \cdot \mathbf{J}(t)$ and $\mathbf{J}(t) = [J_x(t), J_y(t)]$. The resulting HHG spectra are shown in Figs. S10(a)(b) for $\Omega = 1$ and $U = 6$. These data show that the temperature dependence of the HHG intensity is qualitatively the same as that obtained for the Bethe lattice, and the enhancement of the HHG signal with decreasing temperature is independent of the polarization. In Figs. S10(c-f), we show the polarization dependence of the intensity of the HHG peaks for a given order. In the AF phase, the intensity becomes largest when the field is polarized along the bond direction, which is consistent with the experiment on Ca_2RuO_4 ³³. However, interestingly, in the PM phase, the polarization dependence changes qualitatively for the higher harmonic components ($n \geq 5$).

For lower frequencies, like $\Omega = 0.5$ used in the main text, the DMFT self-consistency becomes too expensive for the full simulation of the time evolution. Still, one can simulate halfway, and analyze the subcycle features around the peak of the pulse, see Fig. S11. Again, we find qualitatively the same behavior as in the Bethe lattice, which supports the generality of the physics discussed in the main text.

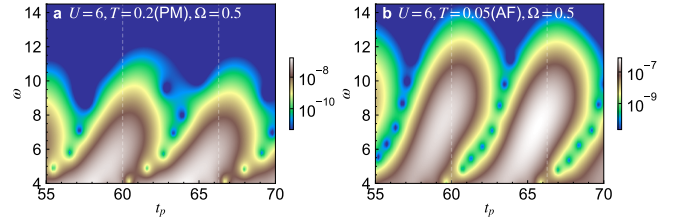


FIG. 11. (a)(b) Subcycle analysis of the HHG signal, $I_{\text{HHG}}(\omega, t_p)$, for the field along the (1,1) direction ($\theta = \pi/4$). Panel (a) is for $T = 0.2$ (PM phase) and (b) is for $T = 0.05$ (AF phase). The pulse parameters are $\Omega = 0.5, E_0 = 0.9\sqrt{2}, t_0 = 60, \sigma = 15$. The vertical dashed lines indicate the times when $E(t) = 0$.

Appendix C: Additional data for the one-dimensional system

In this section, we present supplementary results obtained with iTEBD for the one-dimensional Hubbard model with staggered magnetic field. In Fig. S12, we show how the single-particle spectra change with the magnetic field B_{stagg}^z . One can see that, with increasing field strength, there emerges a separated band at the bottom (top) of the upper (lower) Hubbard band in the momentum-resolved spectrum $A_k(\omega)$. Furthermore,

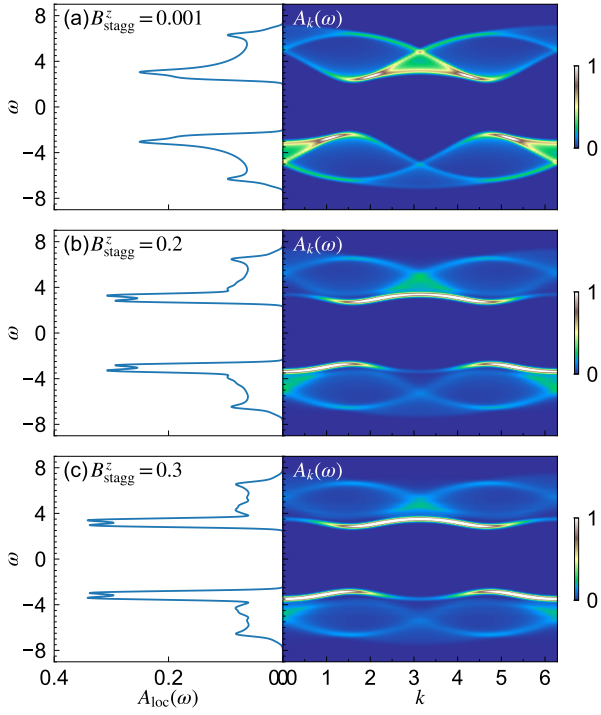


FIG. 12. Momentum-integrated spectrum $A_{\text{loc}}(\omega)$ and momentum-resolved spectrum $A_k(\omega)$ for the one-dimensional Hubbard model with staggered magnetic field at half filling. Panel (a) is for $U = 8$, $B_{\text{stagg}}^z = 0.001$, (b) is for $U = 8$, $B_{\text{stagg}}^z = 0.2$ and (c) is for $U = 8$, $B_{\text{stagg}}^z = 0.3$. Here, we use the iTEBD method.

replicas of these separated bands can be identified. In the momentum-integrated spectrum $A_{\text{loc}}(\omega)$, these subbands correspond to the peaks that emerge with increasing field strength. These features are qualitatively the same as those of the DMFT spectra, and originate from the effective spin-charge coupling and the resulting spin-polarons that are induced by the staggered magnetic field, as mentioned in the main text.